https://doi.org/10.5194/egusphere-2026-2530
Preprint. Discussion started: 8 May 2026

EarthCARE Observations of Vertical Motion and Cloud Microphysical Structure in Tropical Cyclones

Jin-De Huang[1], Woosub Roh[1], Tomoki Miyakawa[1], Masaki Satoh[1, 2]

[1]Atmoshpere and Ocean Research Institute, The University of Tokyo, Chiba, 277-8564, Japan
[2]Typhoon Science and Technology Research Center, Institute for Multidisciplinary Sciences, Yokohama National University, Yokohama, 240-8501, Japan

Correspondence to: Jin-De Hunag (jdhuang@aori.u-tokyo.ac.jp)

Abstract. The Earth Cloud, Aerosol and Radiation Explorer (EarthCARE) satellite mission provides the first spaceborne Doppler radar measurements, enabling new insights into the vertical structure of clouds and precipitation. In this study, we construct a dataset of EarthCARE overpasses of tropical cyclones (TCs) by collocating satellite observations with the International Best Track Archive for Climate Stewardship (IBTrACS). Based on 14 months of observations, we examine the radial structure of radar reflectivity, Doppler velocity, retrieved air motion, and cloud particle types. The results show a transition from convective-like structures in the eyewall to stratiform-like characteristics in the rainband region. The eyewall exhibits stronger updrafts, enhanced reflectivity, and broader Doppler velocity distributions. In contrast, the rainband region shows that weaker vertical motions and Doppler signals are more strongly influenced by hydrometeor fall speeds. We further evaluate TC simulations using the Nonhydrostatic ICosahedral Atmospheric Model (NICAM) with two different cloud microphysical configurations of hydrometeor fall speeds. Both experiments reproduce the overall TC structure but exhibit more confined distributions of radar reflectivity, Doppler velocity, and air velocity compared to the observations. Differences between the two simulations highlight the sensitivity of vertical structure to hydrometeor fall speeds. These results indicate that EarthCARE Doppler observations provide valuable constraints on the coupling between dynamics and cloud microphysics in TCs.

1 Introduction

Understanding vertical motion in cloud systems is crucial for weather forecasting and climate projection, but it has been difficult to observe at fine resolution globally. The Earth Cloud, Aerosol and Radiation Explorer (EarthCARE; Illingworth et al., 2015; Wehr et al., 2023) satellite mission enables observation of vertical motion of clouds for the first time by carrying a 94 GHz nadir-pointing Cloud Profiling Radar (CPR), the first spaceborne Doppler radar to observe cloud and precipitation particles' vertical motion. The EarthCARE also carries 355 nm ATmospheric LIDar (ATLID), with dual-polarization capability, providing information on particle shapes. The unprecedented CPR and ATLID observations enable estimation of hydrometeor fall speed and inference of vertical air motion across diverse cloud regimes (Roh et al., 2026). The detection of

https://doi.org/10.5194/egusphere-2026-2530
Preprint. Discussion started: 8 May 2026

particle shapes by ATLID further improves the understanding of cloud microphysical processes. EarthCARE sheds new light on studies of cloud dynamics and cloud microphysics, which were previously limited in their global observations.

Spaceborne observations have enabled real-time monitoring of tropical cyclones (TCs) and have revealed new insights into TC dynamics before EarthCARE. A geostationary satellite image is used to estimate and forecast the TC intensity of a location (Dvorak, 1975, 1984). Combining cloud top temperature from the Moderate Resolution Imaging Spectroradiometer (MODIS) and cloud top height with CloudSat cloud profiles, Luo et al. (2008) developed a method to better estimate TC intensity. On the other hand, the CloudSat TC dataset (CSTC) has been released and is widely used to understand TC dynamics (Tourville et al., 2015). Using CSTC, Wu and Soden (2017) found that strengthening TCs have 20% higher ice water content (IWC) than weakening TCs. Wu et al. (2020) then showed that the intensification rate is correlated with IWC in rapidly intensifying TCs, suggesting that rapid intensification may be a precursor to TC intensification. Lee and Wing (2024) investigated the role of cloud-radiative feedback in intensifying weak TCs and found that cloud-radiative processes can drive the secondary circulation and enhance TC intensity. The above studies demonstrated a breakthrough in TC understanding using CloudSat observations despite only radar reflectivity. In the era of EarthCARE, by observing with the two active sensors, CPR and ATLID, we can better understand the coupling between dynamics and cloud microphysics in TCs.

In addition to dynamical processes, cloud microphysics plays a crucial role in determining TC structure and evolution. For example, the presence of supercooled liquid water has important implications for latent heat release in the upper levels. Therefore, supercooled water is regarded as the target to weaken TC structure and intensity by seeding during STORMFURY (Willoughby et al., 1985). However, they reported that the changes in TC intensities are limited because TCs contain less supercooled water than expected. Black and Hallett (1986, 1999) showed that supercooled water is hard to find when the temperature is below -5 ℃ due to the efficient depletion by riming and freezing processes. In contrast, aircraft observations of Hurricane Bonnie revealed the presence of large graupel particles at high altitudes, implying in situ growth supported by deeply supercooled cloud droplets within TC updrafts (Black et al., 2003). These contrasting findings highlight the large uncertainties in the occurrence and vertical distribution of supercooled water in TCs. This underscores the need for observational constraints on cloud phase and its coupling with dynamical processes. The cloud particle types retrieved from EarthCARE provide the opportunity to examine the relationship between vertical motion and cloud microphysical structure in TCs.

Recent advances in computational power have enabled the use of global storm-resolving models (GSRMs) to study atmospheric phenomena (Satoh et al., 2019; Stevens et al., 2019). By explicitly resolving deep convection without cumulus parameterization, GSRMs provide explicit representations of the structure and variability of storm systems, including TCs. Judt et al. (2021) analyzed datasets from the nine GSRMs and showed that, while individual models can capture certain aspects of TC behavior, their representations vary across models. Baker et al. (2024) further demonstrated that GSRMs can simulate rapid intensification, which is absent in coarser resolution models with cumulus parameterization. GSRMs can also capture

https://doi.org/10.5194/egusphere-2026-2530
Preprint. Discussion started: 8 May 2026

the sensitivity of the inner-core size to the intensification rate of TCs. These studies highlight the potential of GSRMs for simulating TC, but also indicate the need for further evaluation and development. In particular, observational constraints on both dynamical and cloud microphysical processes of TCs remain limited. The radar reflectivity and Doppler velocity observed by EarthCARE provide a unique opportunity to jointly evaluate and constrain these processes in GSRMs. In Roh et al. (2026), they also argued that the synergetic analysis of EarthCARE and GSRMs could reveal the nature of cloud systems whose understanding is limited solely by EarthCARE or GSRMs.

This study aims to apply unprecedented EarthCARE observations to investigate the dynamical and cloud microphysical structures of TCs, with a particular focus on vertical motion. We co-locate EarthCARE overpasses with TC tracks from the International Best Track Archive for Climate Stewardship (IBTrACS) to construct the EarthCARE-TC dataset following Tourville et al. (2015). In this paper, we analyze 14-month statistics of TC structures observed by EarthCARE and then compare observed TC structures with those simulated by a global storm-resolving model, the Icosahedral Nonhydrostatic Atmospheric Model (NICAM; Tomita and Satoh 2004; Satoh et al., 2008, 2014). The paper is organized as follows: Section 2 describes the data and method; Section 3 presents the results; Section 4 evaluates the model; and Section 5 summarizes the paper.

2 Data and Methodology

2.1 Data

2.1.1 EarthCARE CPR and ATLID

The EarthCARE satellite is a joint mission developed by the European Space Agency (ESA) and the Japan Aerospace Exploration Agency (JAXA). In addition to CPR and ATLID, the EarthCARE satellite carries the Multi-Spectral Imager (MSI) and the Broadband Radiometer (BBR). CPR operates at 94 GHz (W-band) and provides the first spaceborne Doppler radar observation. ATLID is a 355-nm lidar equipped with dual-polarization capability, which enables the observation of particle shape. The retrieved data from the above two sensors are used in this study. We primarily use the JAXA level-2 cloud and precipitation microphysics retrievals from CPR (CPR_CLP; Sato et al., 2025), including radar reflectivity, Doppler velocity, air velocity, cloud water content, and cloud ice content. We also adopt the cloud particle types from the JAXA level-2 CPR-ATLID Synergy Cloud Product (AC_CLP; Sato et al., 2025; Okamoto et al., 2024) to investigate the cloud microphysical structure in TCs and the relationship between vertical motion and cloud microphysics. Both CPR_CLP and AC_CLP data are in the same horizontal (1 km) and vertical (0.5 km) resolutions. We used the data from 1 August 2024 to 31 November 2025 to colocate with TC tracks.

https://doi.org/10.5194/egusphere-2026-2530
Preprint. Discussion started: 8 May 2026

We use radar reflectivity, Doppler velocity, air velocity, terminal velocity, cloud water content, and cloud ice content from the CPR_CLP product, together with cloud particle types from the CPR-ATLID synergy product. Radar reflectivity and Doppler velocity are directly observed variables, while the other quantities are retrieved based on these measurements. For example, cloud water and ice contents are estimated from radar reflectivity using empirical relationships, and air and terminal velocities are derived by decomposing the Doppler velocity, as described by Sato et al. (2009). The cloud particle types are retrieved based on the combined use of CPR and ATLID observations. Cloud particles are categorized into 16 hydrometeor types: missing, clear, warm water, supercooled water, 3D-ice, 2D-plate, mixture of 3D-ice and 2D-plate, liquid drizzle, mixed-phase drizzle, rain, snow, water and liquid drizzle, water and rain, mixed phase, unknown, and melting layer (Okamoto et al., 2024). These retrieval algorithms rely on assumptions regarding particle size distributions, shapes, and scattering properties, which may influence the accuracy of the derived variables in complex cloud conditions. Therefore, uncertainties remain in mixed-phase regions or under conditions of strong attenuation. To reduce uncertainties due to attenuation, we exclude grid points with radar reflectivity values smaller than −20 dBZ, where attenuation effects are significant.

2.1.2 IBTrACS

The TC tracks and TC intensities are adopted from the International Best Track Archive for Climate Stewardship (IBTrACS; Knapp et al., 2010). IBTrACS provides the best-estimated dataset by merging TC records from multiple operational agencies. In this study, we use Version 4r01 of the IBTrACS dataset (Gahtan et al., 2024). The 3-hourly TC position, maximum sustained wind speed, and radius of maximum wind (RMW) are based on the USA agency records. These data are used to identify TC cases intercepted by EarthCARE and to calculate the radial distance from the storm center for composite analyses.

2.1.3 IMERG

Precipitation data are obtained from the Integrated Multi-satellite Retrievals for GPM (IMERG) Final Run product (GPM_3IMERGHH, Version 07). IMERG provides global precipitation estimates by combining observations from multiple passive microwave sensors and infrared measurements, with gauge calibration applied in the Final Run product. The dataset has a temporal resolution of 30 minutes and a spatial resolution of 0.1° × 0.1°. In this study, IMERG data are used to characterize the precipitation structure associated with TCs.

https://doi.org/10.5194/egusphere-2026-2530
Preprint. Discussion started: 8 May 2026

2.2 Methodology

2.2.1 EarthCARE overpass of TCs

To construct a dataset of TC structures observed by EarthCARE, we first identify satellite overpasses that pass within 1000 km of a TC center, following Tourville et al. (2015). The TC position, maximum sustained wind, and RMW are interpolated from the 3-hourly IBTrACS data to the exact EarthCARE overpass time. For each radar profile along the satellite track, the distance to the TC center is calculated and normalized by RMW for subsequent statistical analyses. Figure 1 illustrates an example of the colocation for Hurricane Humberto on 28 September 2025 at 18:17 UTC. Humberto is an intense hurricane over the Atlantic Ocean, reaching Category 4 intensity (Fig. 1a). The EarthCARE ground track intersects Humberto's eye, sampling both the eyewall and outer regions (Fig. 1b). At the time of the overpass, Humberto was undergoing an eyewall replacement process. The cross section of radar reflectivity (Fig. 1c) shows strong signals within ±100 km of the storm center, indicating substantial condensate in the eyewall and rainband regions. The Doppler velocity field (Fig. 1d) reveals updraft structures associated with the double eyewall, with the inner eyewall located near 9 km (closest point) and the outer eyewall near ±50 km. Stronger and more concentrated upward Doppler velocity in the inner eyewall compared to the outer eyewall. Beyond ±100 km, isolated convection and anvil cloud structures are observed in the outer region. Figure 1e shows the retrieved cloud particle types from the CPR-ATLID synergy product. Rain dominates below the freezing level, while snow particles are associated with regions of enhanced reflectivity. In the upper troposphere, 3-D ice particles are prevalent, particularly in the anvil region. These cross sections demonstrate the capability of EarthCARE to capture the vertical structure of clouds and Doppler velocity within a TC.

https://doi.org/10.5194/egusphere-2026-2530
Preprint. Discussion started: 8 May 2026

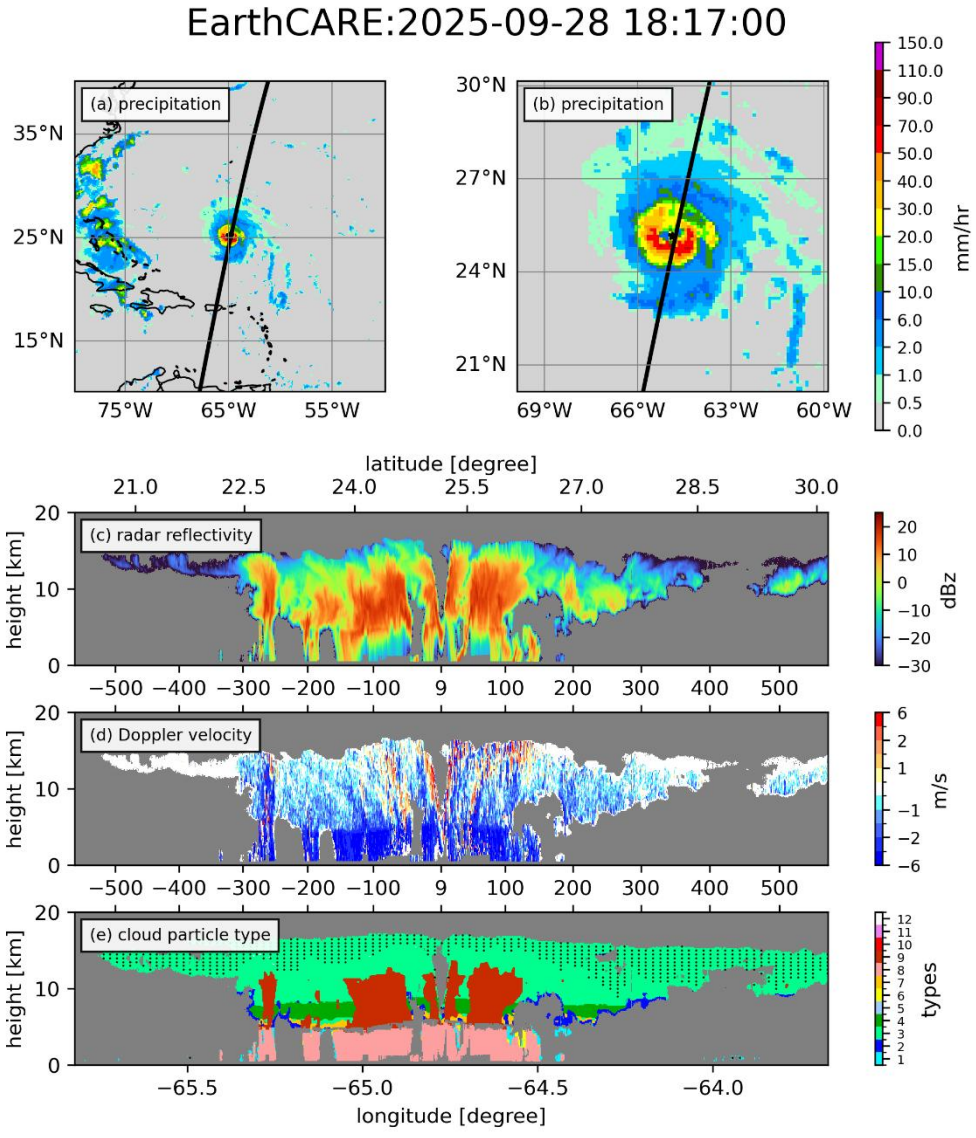

Figure 1. (a) and (b) are IMERG precipitation accumulated from 18Z to 19Z for large and small domain, respectively. The black line indicates the track of EarthCARE overpass. (c) demonstrates the cross-section of radar reflectivity in (b). (d) is the same but for Doppler velocity. (e) shows the retrieved cloud particle types: 1, warm water; 2, supercooled water; 3, 3-D ice; 4, 2-D plate; 5, mixture of 3-D ice and 2-D plate; 6, liquid drizzle; 7, mixed-phase drizzle; 8, rain; 9, snow; 10, water and liquid drizzle; 11, water and rain; and 12, mixed phase. The types of clear, melting layer, and missing are not shown here. Distances (km) from the TC center are indicated between panels (c)-(d) and (d)-(e).

https://doi.org/10.5194/egusphere-2026-2530
Preprint. Discussion started: 8 May 2026

2.2.2 NICAM hindcast simulations

NICAM is used to perform hindcast simulations in this study. The model is configured with a horizontal resolution of approximately 3.5 km and 78 vertical levels using a terrain-following coordinate. The vertical grid spacing increases from 66 m near the surface to 400 m at 3.3 km, remains constant up to 18 km, and then increases toward the model top at 50 km. Cloud microphysical processes are represented using the NICAM Single-moment Water 6 (NSW6; Tomita, 2008; Roh et al., 2014) scheme, which includes six prognostic hydrometeor species. Radiative transfer is calculated using the MSTRNX scheme based on the correlated k-distribution method (Sekiguchi and Nakajima, 2008). Surface processes are represented by the MATSIRO land surface model (Takata et al., 2003) and a slab ocean model, while subgrid-scale turbulence is parameterized using the Mellor-Yamada-Nakanishi-Niino level 2 scheme (MYNN2; Nakanishi & Niino, 2006; Noda et al., 2010).

The simulations are initialized at 00:00 UTC on 27 September 2025 using atmospheric initial conditions interpolated from the ERA5 reanalysis, while sea surface temperature is nudged toward daily Optimum Interpolation Sea Surface Temperature (OISST) in the slab ocean model, with a 7-day relaxation time to prevent SST drift. Land initial conditions are taken from climatology derived from a low-resolution NICAM simulation. Each simulation is integrated for 2 days, with output frequencies of 3-hourly for three-dimensional variables and 1-hourly for two-dimensional fields. In this study, we use the Joint-Simulator for satellite sensors (J-Sim; Hashino et al., 2013; Roh et al., 2025) to produce the EarthCARE CPR-like signals of radar reflectivity and Doppler velocity based on NICAM outputs, which can be directly compared to the EarthCARE signals.

Two simulations are performed with different cloud microphysical settings: the HighResMIP-tuned configuration (Kodama et al., 2021; hereafter K21) and the global K-scale climate configuration (Takasuka et al., 2024; hereafter T24). The primary difference between K21 and T24 lies in the coefficients used to parameterize the terminal velocities of hydrometeors. K21 applies larger coefficients for terminal velocities of snow and rain, while cloud ice is assumed to be non-falling. In contrast, T24 uses smaller parameters for snow and rain and assigns a small constant fall speed (0.1 m s^{-1}) to cloud ice. Additionally, T24 incorporates lateral moisture mixing through the Leonard term. Sensitivity experiments using these two different cloud microphysics schemes provide an insightful framework for examining how simulated radar reflectivity and Doppler velocity, that is, the dynamics and cloud microphysics within a TC, respond to changes in terminal speeds of hydrometeors.

https://doi.org/10.5194/egusphere-2026-2530
Preprint. Discussion started: 8 May 2026

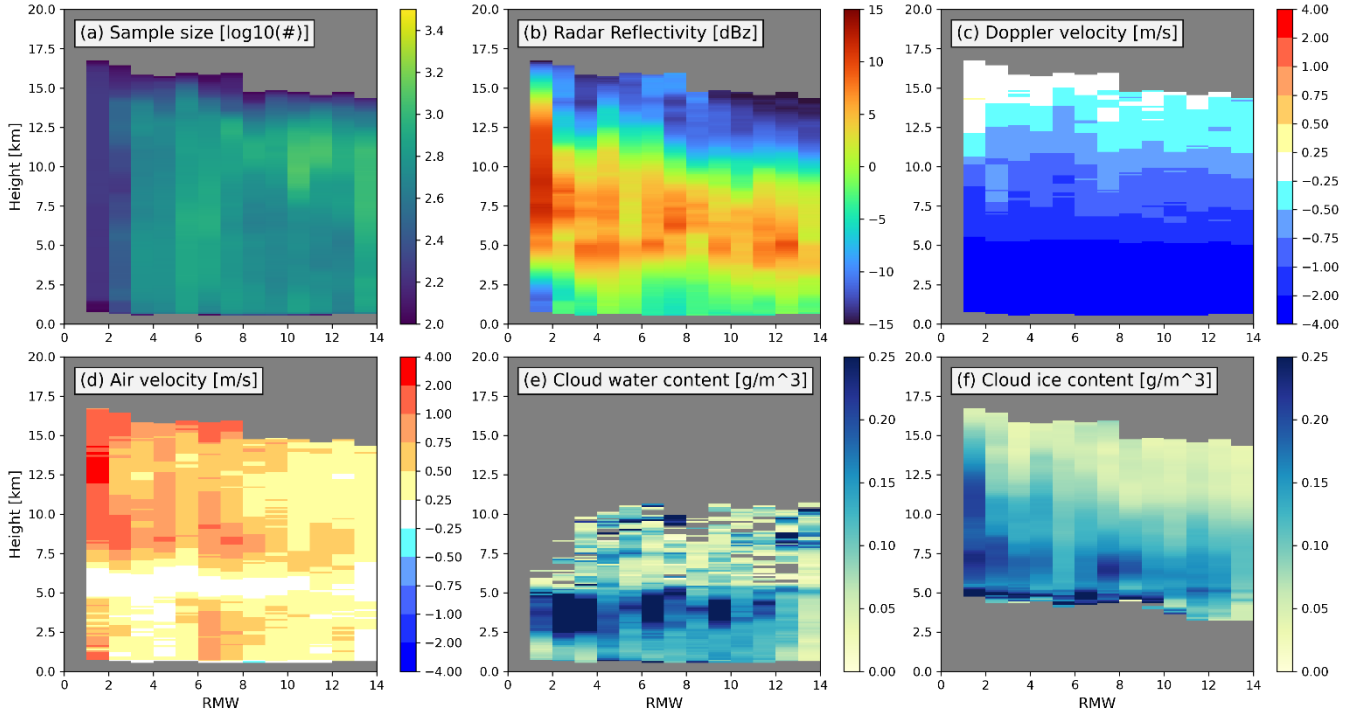

Figure 2. Radial composites based on RMW of (a) sample size [log10(#)], (b) radar reflectivity [dBz], (c) Doppler velocity [m s^{-1}], (d) air velocity [m s^{-1}], (e) cloud water content [g m^{-3}] , and (f) cloud ice content[g m^{-3}]

3 Observational Analysis

3.1 Radial Composites of Tropical Cyclones

Figure 2 presents the radial-height composite structure of strong TCs (maximum wind speed > 94 knots, Category 3 and above). The sample size indicates sufficient observational coverage from 2 to 15 RMW (Fig. 2a). Radar reflectivity (Fig. 2b) reveals a coherent vertical structure characterized by enhanced echoes in the eyewall region (RMW < 2), where strong reflectivity extends to 12.5 km. The upper extent of strong reflectivity decreases sharply at 2 RMW, marking the transition from the eyewall to the primary rainband region. A relative minimum in reflectivity at 5 RMW suggests a separation between the primary and outer rainband regions. In the rainband region (2–5 RMW), reflectivity above 5 km is slightly weaker than in the eyewall, while a pronounced reflectivity layer near 5 km corresponds to the melting layer. Beyond 5 RMW (outer region), both the intensity and vertical extent of reflectivity decrease gradually with increasing distance from the TC center. Overall, the composite structure derived from the EarthCARE observation is consistent with the canonical organization of TCs, including a deep convective inner core and progressively weaker outer rainbands. Three radial regions are defined based on

https://doi.org/10.5194/egusphere-2026-2530
Preprint. Discussion started: 8 May 2026

RMW: the eyewall (R < 2 RMW), the rainband (2–5 RMW), and the outer region (5–15 RMW). These definitions are used throughout the following analysis.

Doppler velocity shows predominantly negative values below 15 km (Fig. 2c), with a broadly similar vertical structure across radial regions. Above the freezing level (~5 km), Doppler velocity increases from approximately -2 m s^{-1} to near 0 m s^{-1} with height. Below the freezing level, Doppler velocities become more negative, reaching around -4 m s^{-1}, consistent with the contribution of liquid particle fall speeds in the lower troposphere. Air vertical velocity exhibits upward motion in the mid-to-upper troposphere (Fig. 2d). A layer of near-zero vertical velocity is observed around 5-7 km across all regions, in which the retrieval of vertical motion in mixed-phase conditions may be uncertain (see Section 4). Stronger upward motion is evident in the eyewall between approximately 7.5 and 15 km height, while upward motion is more confined to 7.5-12.5 km height in the rainband region. Beyond 5 RMW, the magnitude of upward motion generally decreases. Notably, localized upward motion is also observed below the freezing layer in the eyewall and in parts of the outer region (6-8 RMW). The vertical structure of air motion in the eyewall and outer regions resembles convective updrafts, except for a gap that may be due to retrieval uncertainties in the mixed-phase layer. On the other hand, the rainband region shows a more stratiform structure, characterized by the bright band signal and top-heavy vertical motions.

The distributions of the retrieved cloud water and cloud ice further illustrate the cloud microphysical structure of TCs (Fig. 2e and 2f). Cloud water is primarily confined to the lower troposphere below approximately 5 km, while cloud ice dominates the upper troposphere above this level. Between 5-10 km, mixture of ice and liquid phases is presented, indicating the existence of supercooled water. Within the region RMW less than 8, cloud water is most pronounced between approximately 2.5 and 5 km, while the occurrence decreases both above and below this layer. Cloud water is also detected above 5 km, indicating the presence of supercooled liquid water up to approximately 10 km. However, its occurrence is relatively limited, suggesting that it does not dominate the composite structure at these levels. Below approximately 2.5 km, cloud water retrieval may be affected by attenuation, potentially leading to an underestimation of liquid water content near the surface. The distribution of cloud ice generally follows that of radar reflectivity, with enhanced ice content in regions of stronger reflectivity. The distributions of cloud water and ice contents provide cloud microphysical structures in TCs for further model evaluations.

https://doi.org/10.5194/egusphere-2026-2530
Preprint. Discussion started: 8 May 2026

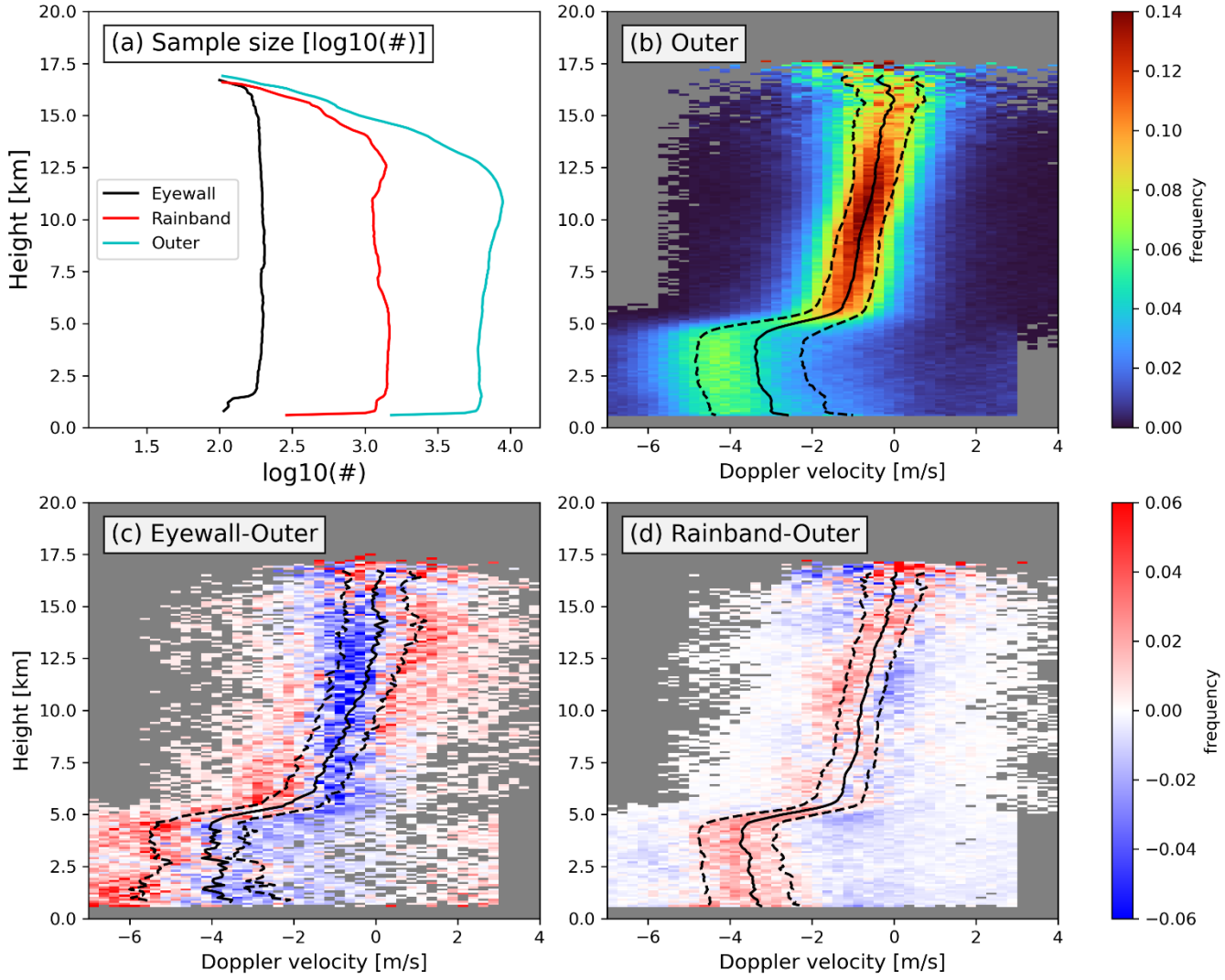

Figure 3. (a) sample size of three different regions. (b) PDF of Doppler velocity for the outer region (5<RMW<15). PDF of (c) eyewall and (d) rainband regions, respectively, relative to the outer region. Solid lines represent the mean of Doppler velocity, while dashed lines indicate interquartile range.

3.2 Doppler and Air velocity

Based on the structural differences identified in Fig. 2, the samples are divided into eyewall, rainband, and outer regions to examine the distribution of vertical motion in more detail. The sample size in each region exceeds 100 across most vertical levels (Fig. 3a), providing sufficient coverage for statistical analysis. The Doppler velocity probability density function (PDF) in the outer region is used as a reference (Fig. 3b). A sharp transition in Doppler velocity at around 5 km in height indicates

https://doi.org/10.5194/egusphere-2026-2530
Preprint. Discussion started: 8 May 2026

the melting level, which separates the ice- and liquid-phase particle layers. Above the melting level, the PDF is relatively symmetric and concentrated within the interquartile range, resembling a near-normal distribution. In contrast, below the melting level, the PDF becomes broader and skewed toward negative velocities, with a mean around −3 m s^{-1} and a peak near −4 m s^{-1}. The eyewall region exhibits a substantially broader distribution compared to the outer region (Fig. 3c). Below the melting level, the distribution shifts with enhanced frequency at both more negative (−6 m s^{-1}) velocities. Between 5 and 7.5 km, PDF shifts to a more negative region. Above 7.5 km, the frequency decreases within the interquartile range and increases toward higher Doppler velocities, suggesting enhanced upward motion. In the rainband region (Fig. 3d), the Doppler velocity distribution is systematically shifted toward more negative values relative to the outer region. The frequency increases on the negative side and decreases on the positive side across most altitudes. To summarize, the Doppler velocity distributions exhibit distinct characteristics across radial regions: a broadened distribution in the eyewall, a negatively shifted distribution in the rainband, and a relatively narrow distribution in the outer region.

https://doi.org/10.5194/egusphere-2026-2530
Preprint. Discussion started: 8 May 2026

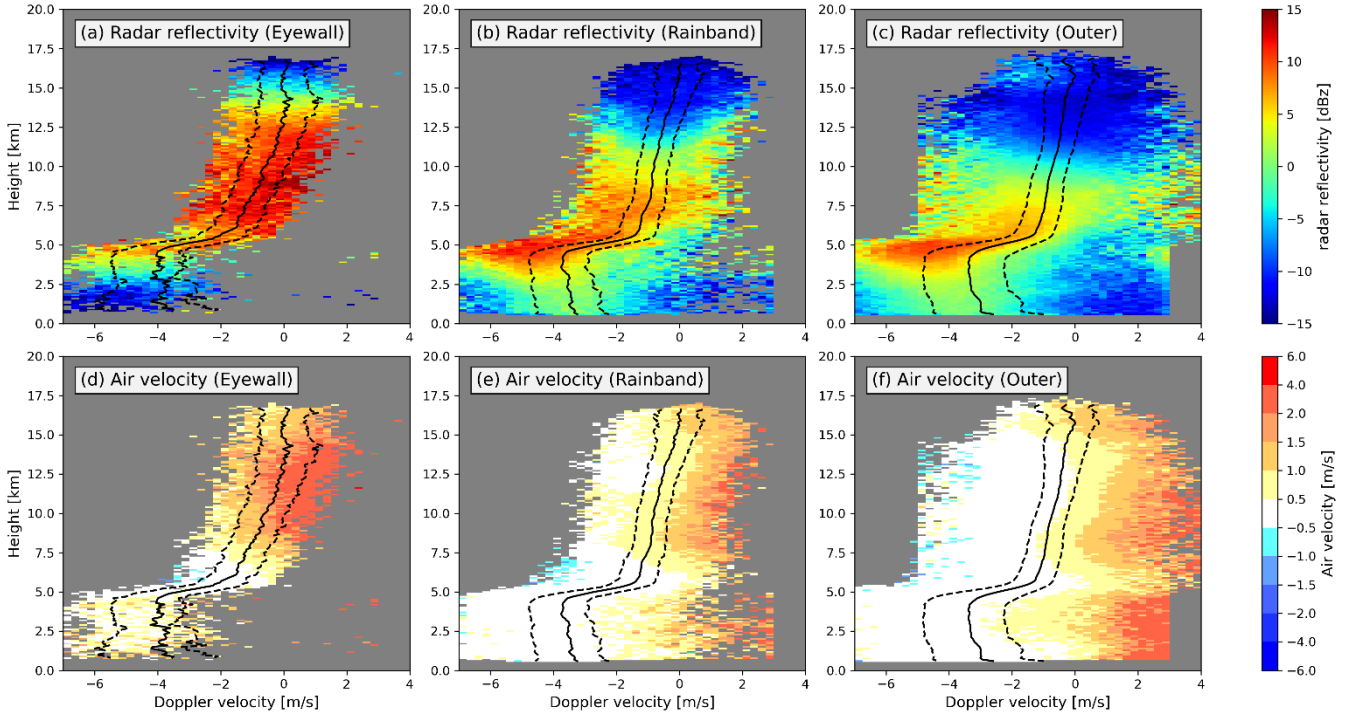

Figure 4. The composite of radar reflectivity (a, b, and c) and air velocity (d, e, and f) on the Doppler velocity bins for (a and d) eyewall, (b and e) rainband, and (c and f) outer regions. Solid lines represent the mean of Doppler velocity, while dashed lines indicate interquartile range. We eliminate the points where sample size less than 5.

We examine the conditional distributions of radar reflectivity and air vertical velocity (Fig. 4). In the eyewall region, enhanced radar reflectivity is primarily observed above the freezing level, while weaker signals below are likely influenced by attenuation from overlying dense clouds (Fig. 4a). Strong reflectivity is preferentially associated with Doppler velocities greater than the upper quartile, indicating that cloud particles tend to coincide with upward anomalies of Doppler velocity. This behavior is consistent with convective updraft structures. In the rainband region, strong reflectivity is mainly located at Doppler velocities smaller than the mean around the freezing level (Fig. 4b). Above 6 km, enhanced reflectivity is generally associated with Doppler velocities below the upper quartile, suggesting that Doppler velocity in the rainband is contributed by the particle falling. The significant signal near the freezing level indicates a radar-bright band, consistent with stratiform precipitation. In the outer region, reflectivity is generally weaker than in the rainband and is largely confined near the freezing level (Fig. 4c).

The conditional distributions of air vertical velocity show consistent differences across regions. In the eyewall, upward motion above the freezing level within the interquartile range reaches approximately 1–2 m s^{-1}, and stronger updrafts (>2 m s^{-1}) occur

https://doi.org/10.5194/egusphere-2026-2530
Preprint. Discussion started: 8 May 2026

at Doppler velocities greater than the upper quartile (Fig. 4d). These updrafts tend to coincide with regions of enhanced reflectivity. In contrast, in the rainband, vertical motion within the interquartile range is weaker (approximately 0.5 m s^{-1}) and shows little correspondence with regions of strong reflectivity (Fig. 4e). In the outer region, vertical motion is generally weak across the Doppler velocity range (Fig. 4f). Below the freezing level, weak upward motion is observed in the eyewall across a wide range of Doppler velocities, whereas in the rainband and outer regions, upward motion primarily occurs at Doppler velocities greater than the upper quartile. Overall, these results indicate that the eyewall is characterized by strong coupling between upward motion and precipitation, consistent with convective structures, while the rainband and outer regions exhibit features more consistent with stratiform precipitation, including a pronounced bright band and weaker coupling between reflectivity and vertical motion.

https://doi.org/10.5194/egusphere-2026-2530
Preprint. Discussion started: 8 May 2026

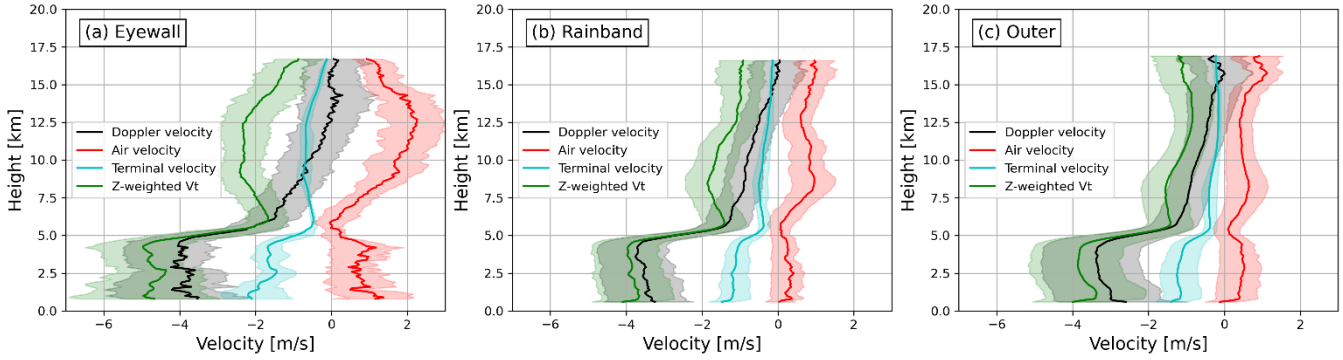

Figure 5. The means and interquartile ranges of Doppler velocity, air velocity, terminal velocity, and radar reflectivity-weighted terminal velocity in (a) eyewall, (b) rainband, and (c) outer regions.

We further quantify the relative contributions of air motion and particle fall speed, which vary across three regions (Fig. 5). Doppler velocity is defined as

$$V_D = V_{air} + V_{tz} + E \ (1),$$

where V_{air} is the air velocity, V_{tz} is the radar reflectivity-weighted terminal velocity of particles, and E is the uncertainty from observation and retrieval processes. Here we show the terminal velocity, which is retrieved from V_{tz} depending on particle size, shape, orientation, and temperature. V_{tz} is not provided in the CPR product, so we use an estimate of $V_D - V_{air}$ for interpretation. In the eyewall region, terminal velocities above 6 km are slightly larger and exhibit a broader interquartile range than in the rainband and outer regions (Fig. 5a), indicating a large variability of ice particle size. Consequently, V_{tz} is more negative, reflecting the contribution of larger and faster-falling particles. The negative V_{tz} is offset by strong upward air motion, which results in the Doppler velocity close to 0 m s^{-1}. In the rainband region, the air vertical motion is weaker than in the eyewall region (Fig. 5b) and is not large enough to offset the contribution from ice particle terminal velocity, which is slightly faster than that in the outer region. As a result, the overall PDF of Doppler velocity in ice phase shifts toward more negative values compared to the outer region (Fig. 3d). In the outer region, the terminal velocity of ice particles is slowest and has the smallest interquartile range among the three regions (Fig. 5c). The air vertical velocity is also weakest, leading to intermediate values of Doppler velocity. Below the freezing level, Doppler velocity is mainly controlled by the fall speed of liquid particles, while the contribution from air motion is limited. The air motion in the rainband region is the weakest among the three regions. Overall, in the eyewall region, strong updrafts, faster terminal velocities, and the greater variance in terminal velocity are consistent with convective characteristics. In contrast, in the rainband region, weaker air motion below the freezing level and the presence of a bright band are more consistent with stratiform characteristics.

https://doi.org/10.5194/egusphere-2026-2530
Preprint. Discussion started: 8 May 2026

3.3 Cloud Particle Type

We investigate the distribution of cloud particle types, retrieved from both CPR and ATLID, to further understand the cloud microphysical structures in TCs. The radial-height frequency diagrams of different particle types are shown in Fig. 6. We first categorize these cloud particle types into 5 groups: small ice, small liquid, mixed-phase, snow, and rain groups. The small ice particle group (Fig. 6a) includes 3D ice, 2D plates, and mixtures of these types, while the mixed-phase group (Fig. 6c) includes supercooled water, mixed-phase drizzle, and mixed-phase types. The distribution of cloud particle types exhibits a clear vertically stratified structure. Small ice particles dominate above 12 km across all regions (Fig. 6a). Between 5 and 12 km, snow particles are most prominent in the eyewall region, whereas the rainband region contains a mixture of small ice particles and snow (Fig. 6b). This pattern is consistent with the difference in terminal velocities identified between the eyewall and rainband regions (Fig. 5a and 5b). In the outer region, the occurrence of snow particles decreases and is largely confined below 10 km. Mixed-phase particles mainly occur between 5 and 7.5 km (Fig. 6c), which may contribute to the uncertainty in retrieving both terminal velocity and air motion. These particles are more frequently observed in the outer region (5<RMW<10). Below the freezing level (~5 km), rain is the dominant hydrometeor type (Fig. S1). Small liquid particles, including warm water, water and liquid drizzle, water and rain, and liquid drizzle, are rare within RMW < 5 but show a slight increase in occurrence in the outer region (Fig. 6d).

https://doi.org/10.5194/egusphere-2026-2530
Preprint. Discussion started: 8 May 2026

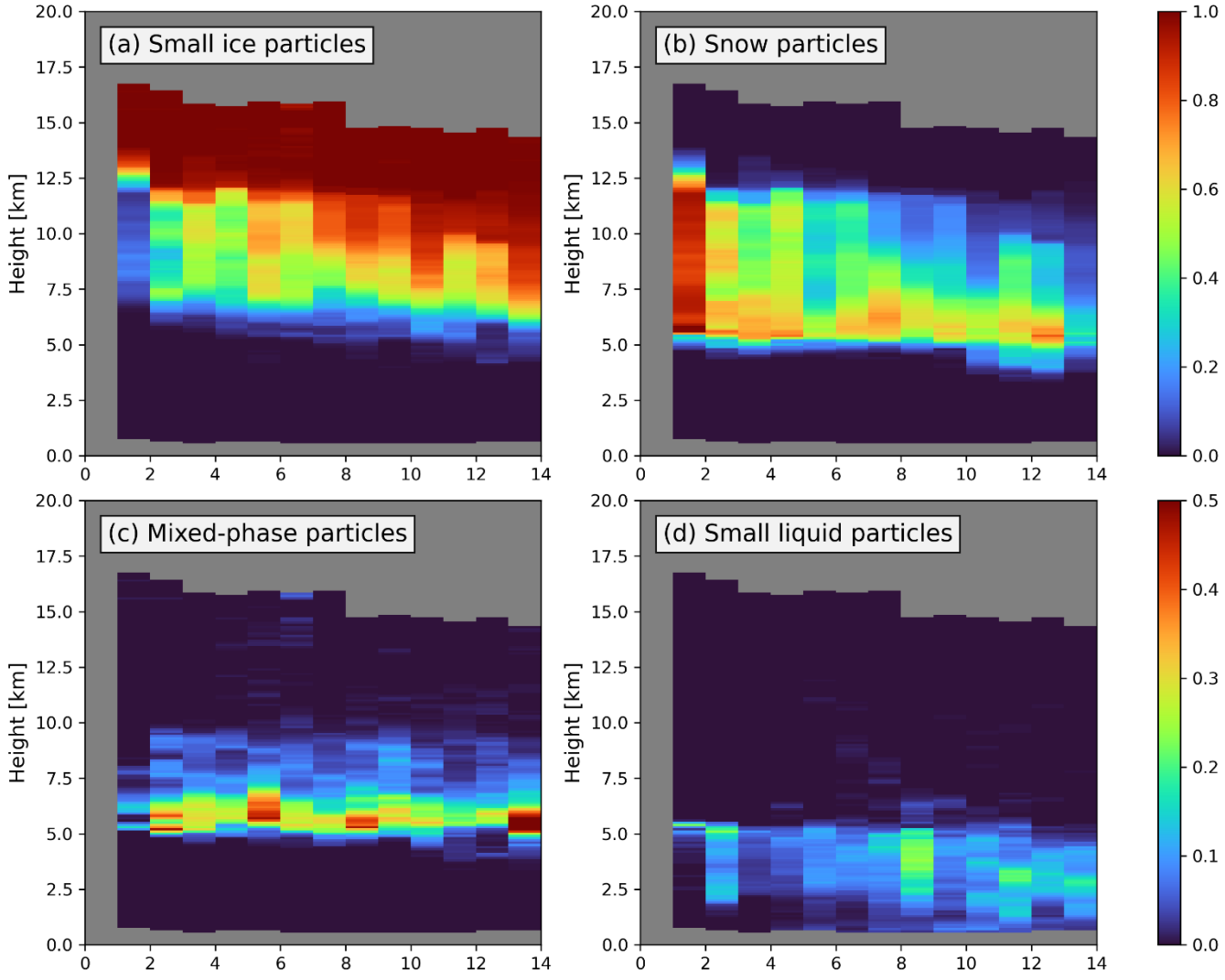

Figure 6. RMW-height frequency diagram of (a) small ice, (b) snow, (c) mixed-phase, and (d) small liquid particles.

315

https://doi.org/10.5194/egusphere-2026-2530
Preprint. Discussion started: 8 May 2026

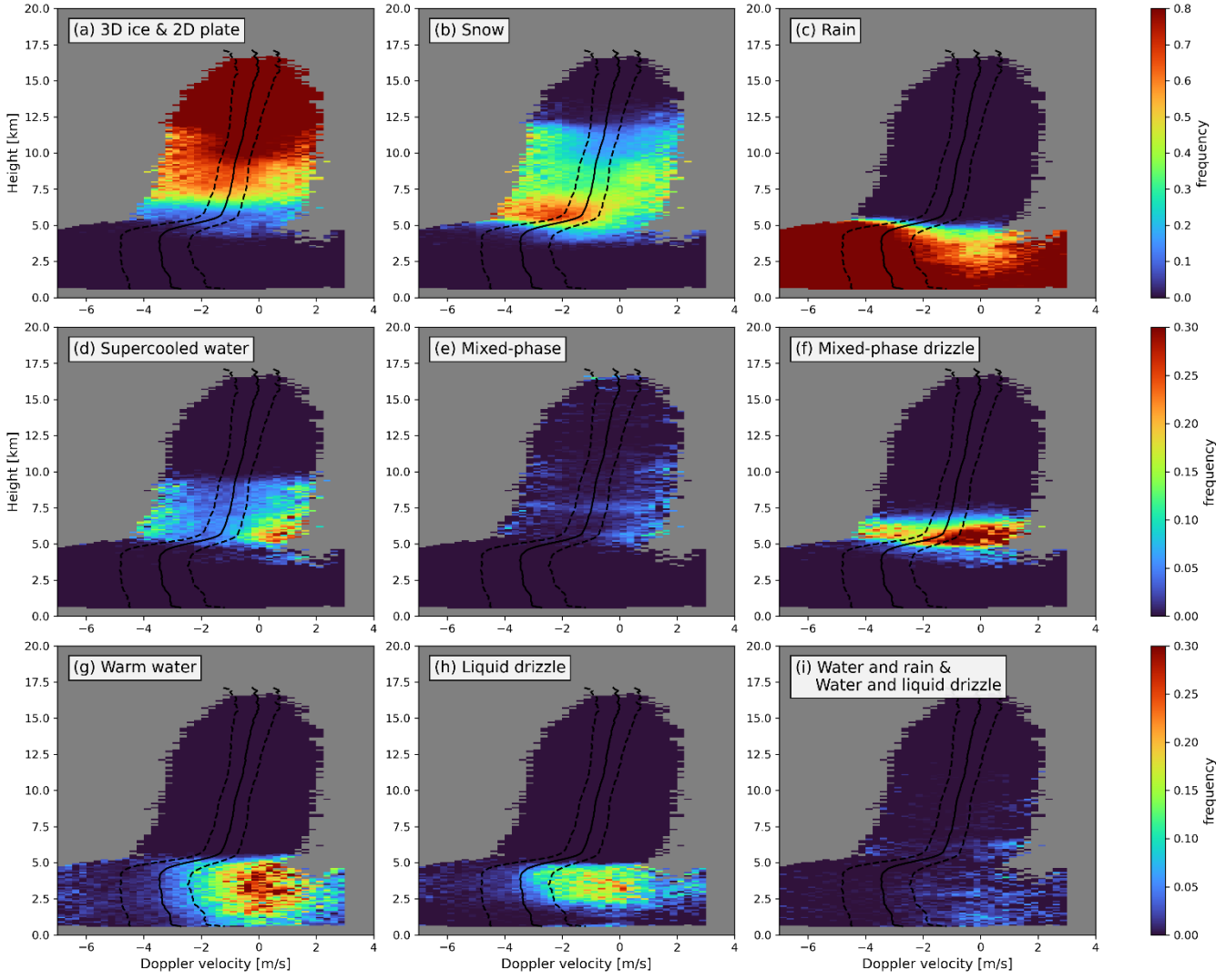

Figure 7. Frequency diagrams of (a) 3D ice & 2D plate, (b) snow, (c) rain, (d) supercooled water, (e) mixed-phase, (f) mixed-phase drizzle, (g) warm water, (h) liquid drizzle, and (i) water & rain on the DPF of Doppler velocity.

320

https://doi.org/10.5194/egusphere-2026-2530
Preprint. Discussion started: 8 May 2026

We further project the frequency diagrams onto Doppler velocity PDFs to investigate the relationship between Doppler velocity and cloud particle types. Because the sample size in the eyewall region is insufficient for conditional sampling, all three regions are combined to construct the frequency diagrams in Doppler velocity space (Fig. 7). The upper panels show the dominant cloud particle types: small ice particles, snow, and rain. The combination of 3D ice and 2D plates dominates above 7.5 km, except in regions beyond the upper quartile of Doppler velocity (Fig. 7a). In these regions, snow and supercooled water are present, although with lower frequency (Fig. 7b and 7d). Below the freezing level, rain is the dominant particle type (Fig. 7c). However, its frequency decreases in the region of Doppler velocity close to 0 m s^{-1}, where warm water and liquid drizzle become more evident (Fig. 7g and 7h).

The lower panels of Fig. 7 highlight particle types that mainly occur beyond the upper quartile, corresponding to upward motion identified in Fig. 4. Mixed-phase particles are relatively rare but exhibit a distribution along the edges of the Doppler velocity PDF (Fig. 7e). Mixed-phase drizzle frequently occurs slightly above the freezing level, but is also found in regions beyond the lower quartile (Fig. 7f). All mixed-phase particles, including supercooled water, mixed phase, and mixed-phase drizzle, indicates enhanced occurrences at both more negative and less negative (or near-zero) Doppler velocities. The more negative Doppler velocities are associated with larger hydrometeor fall speeds, likely reflecting enhanced particle growth processes such as riming. On the other hand, the less negative or near-zero Doppler velocities correspond to upward air motion. The coexistence of these two regimes suggests that mixed-phase processes are closely linked to dynamical conditions. In particular, the occurrence of supercooled water and mixed-phase particles in regions of upward motion implies that riming processes are likely enhanced within convective updrafts, where supercooled liquid water is available. The combined water and rain category occurs infrequently at lower levels (Fig. 7i). These results show that the occurrence of different particle types is systematically linked to Doppler velocity, reinforcing that Doppler velocity provides constraints on both particle phase and vertical structure, as well as the coupling between dynamical and microphysical processes in TCs.

https://doi.org/10.5194/egusphere-2026-2530
Preprint. Discussion started: 8 May 2026

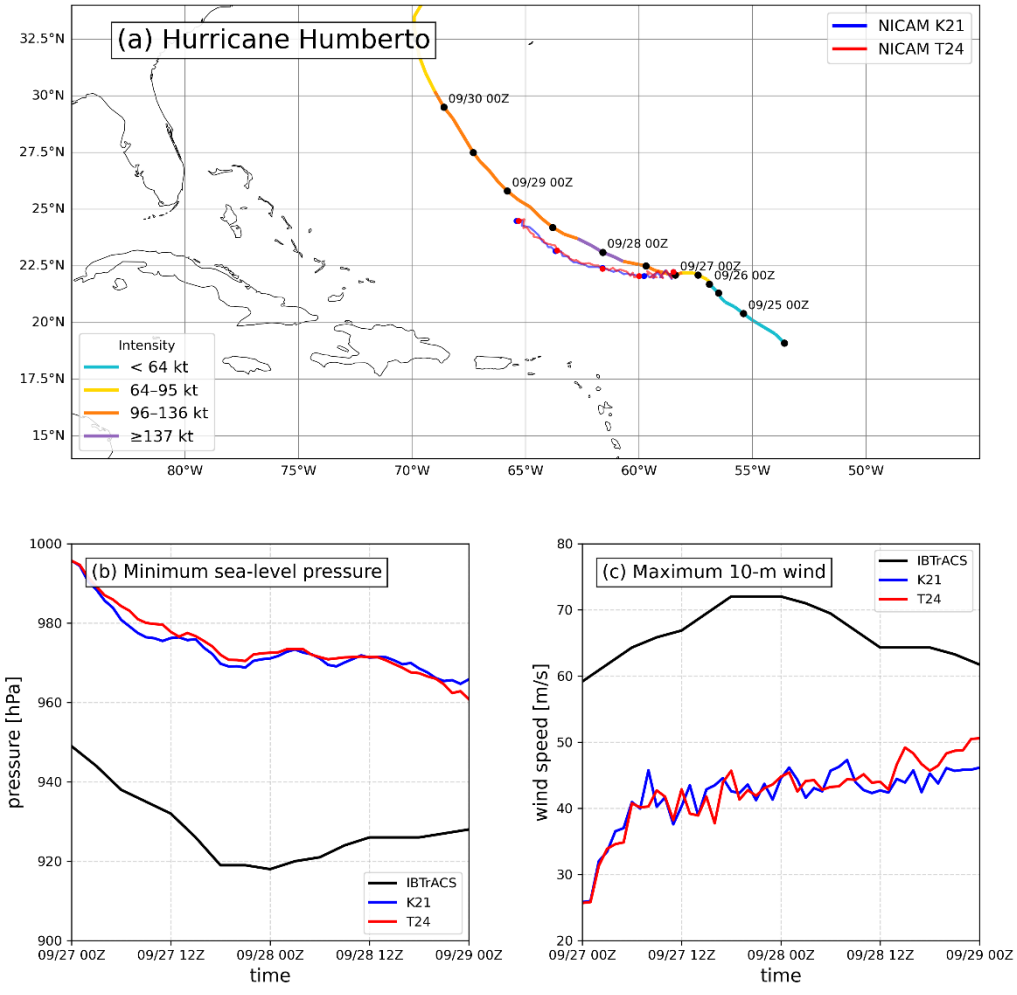

345 Figure 8. (a) Tracks of IBTrACS, K21, and T24. Time evolutions of (b) minimum sea-level pressure and (c) maximum near-surface wind.

https://doi.org/10.5194/egusphere-2026-2530
Preprint. Discussion started: 8 May 2026

4 Model Evaluation

4.1 Simulated Hurricane

As a representative case study, we conduct NICAM hindcast simulations of Hurricane Humberto and evaluate the results using EarthCARE observations (Fig. 1). Figure 8 compares the simulated track and intensity evolution of Hurricane Humberto with IBTrACS data. Both simulations reproduce the observed track reasonably well (Fig. 8a), although a slight southward bias is present. The storm intensity is substantially underestimated in both simulations, with higher central pressure and weaker maximum wind speeds than IBTrACS (Fig. 8b and c). The track bias and intensity underestimation may be partly related to limitations in the initial conditions and initialization procedure. In particular, the coarse resolution of the ERA5 reanalysis (0.25°) does not fully capture the intensity of Humberto, with the minimum sea-level pressure slightly below 1000 hPa (Fig. 8b), and spin-up effects remain a known challenge for the NICAM simulations. Despite these limitations, the two simulations provide a useful basis for comparison with EarthCARE observations. The differences between K21 and T24 are relatively small, with T24 producing slightly stronger winds and lower central pressure during the final 6 hours of the simulations.

https://doi.org/10.5194/egusphere-2026-2530
Preprint. Discussion started: 8 May 2026

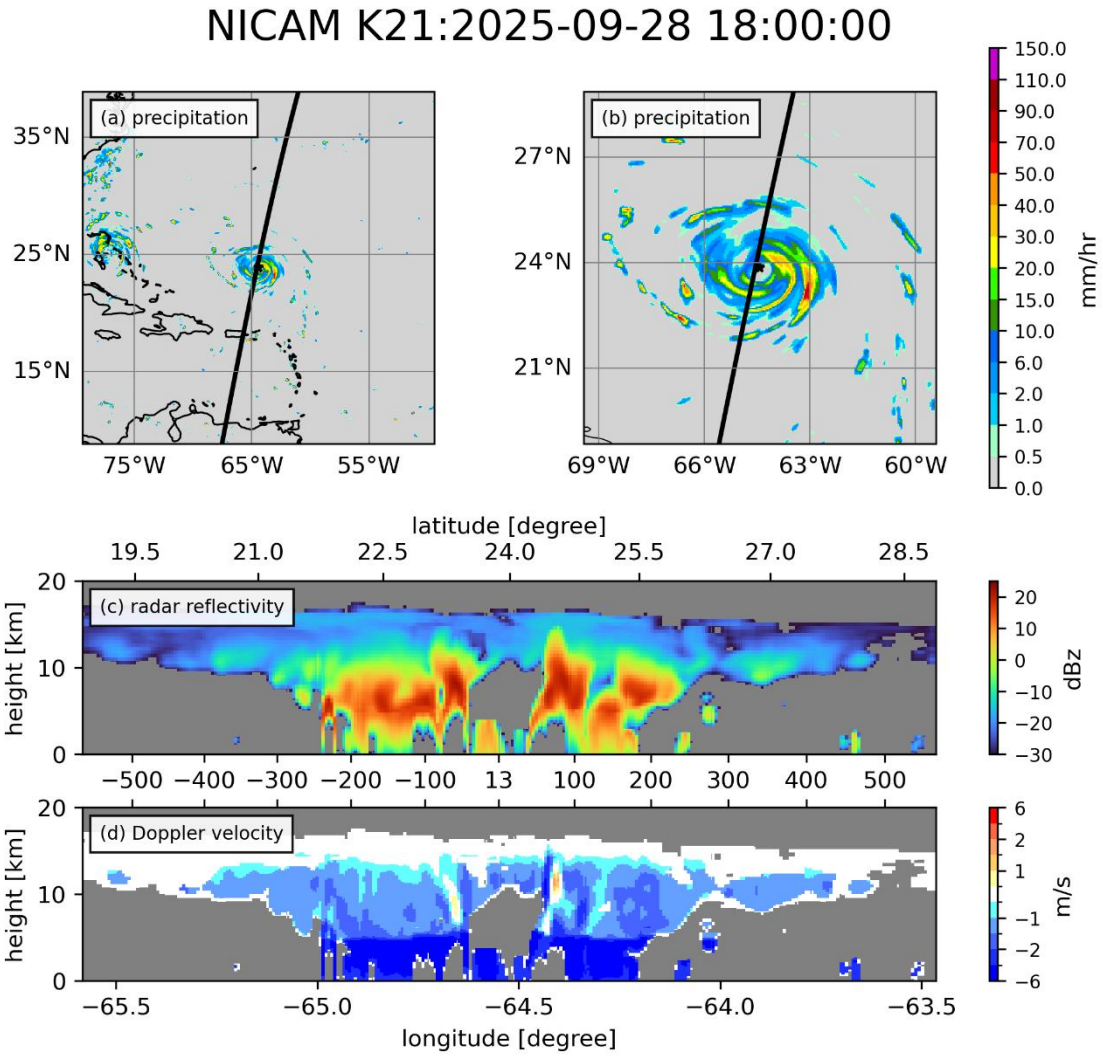

Figure 9. (a) and (b) are NICAM precipitation accumulated from 18Z to 19Z for large and small domain, respectively. The black line indicates the track of EarthCARE overpass with 0.5-degree eastward shift. (c) demonstrates the cross-section of simulated radar reflectivity in (b). (d) is the same but for simulated Doppler velocity.

Figure 9 shows the simulated radar reflectivity and Doppler velocity generated by the J-Sim along the EarthCARE overpass. To facilitate comparison, the EarthCARE overpass is shifted 0.5° eastward to intersect the simulated eyewall (Fig. 9a). Here, we present results from K21, while those from T24 are provided in the supporting information. The simulated precipitation pattern is sparser than that in the IMERG observations, and the rainfall intensity in the eyewall region is weaker in K21 (Fig. 9b and 1b). Despite this, the simulated radar reflectivity captures the overall storm structure, including deep convective and stratiform regions extending into the upper troposphere (Fig. 9c). Compared to observations, the simulated reflectivity is

https://doi.org/10.5194/egusphere-2026-2530
Preprint. Discussion started: 8 May 2026

generally stronger but vertically confined below 10 km (Fig. 9c and 1c). Below the freezing level, radar reflectivity is substantially attenuated in both observations and simulations. The simulated Doppler velocity shows more negative values above the freezing level compared to observations (Fig. 9d and 1d). NICAM reproduces the overall TC structure, but notable discrepancies remain in both the intensity and vertical structure when compared with EarthCARE observations.

We compare the joint PDFs of radar reflectivity, Doppler velocity, and air velocity between EarthCARE observations and NICAM simulations (Fig. 10). Here, we only use the cross-section of data to perform statistics to fairly compare with EarthCARE, and the result using all data in NICAM can be found in the supplement (Fig. S2 and S3). The observed distributions exhibit a broad spread across all variables, reflecting substantial variability in both dynamical and cloud microphysical processes. In contrast, the simulated PDFs are much more confined. We focus on the structure above the freezing level because the signal is significantly attenuated below this level. Figure 10a shows that the EarthCARE PDF has a peak occurrence between 10 and 15 dBz and develops a double-peaked structure with increasing height. One peak remains near 10 dBz and sharply shifts toward lower reflectivity at 12.5 km, while the other one tilts from about 5 dBz at 7 km to −10 dBz at 12.5 km. In both K21 and T24, the PDF peaks occur between 15 and 20 dBz at around 6 km, indicating an overestimation of radar reflectivity (Fig. 10b and 10c). Moreover, the simulated reflectivity does not reproduce the double-peaked structure observed by EarthCARE. With sufficient sampling, T24 tends to reproduce a double-peaked structure; however, the separation between the two peaks is less distinct in the PDF (Fig. S2). With increasing height, the peak in K21 shifts rapidly from ~15 dBz at 6 km to −15 dBz at 12 km. The peak in T24 remains near 15 dBz up to 8 km and decreases more gradually, reaching −10 dBz at around 14 km. However, T24 exhibits a narrower PDF between 8 and 12.5 km compared to K21. These results suggest that the smaller terminal velocity coefficients in T24, which reduce particle fall speeds, can improve the PDF structure with a more gradual vertical transition, even though its PDF becomes narrower than K21.

The PDF of Doppler velocity observed by EarthCARE shifts from about −1.5 m s^{-1} at 5 km to −0.5 m s^{-1} at 15 km (Fig. 10d). In K21, the peak of the PDF is well captured near −1.5 m s^{-1} at 5 km, but the peak remains near −1.5 m s^{-1} from 5 to 12.5 km and then rapidly shifts toward −0.5 m s^{-1} (Fig. 10e). The result suggests an overestimation of ice particle terminal velocities. In contrast, the peak in T24 remains around −0.5 m s^{-1} throughout most of the vertical range in ice phase (Fig. 10f). These differences indicate that changes in the terminal velocity coefficients substantially affect the vertical structure of Doppler velocity. On the other hand, the PDFs of air velocity in both K21 and T24 are much narrower than those observed by EarthCARE (Fig. 10g–i). This suggests that the simulations underestimate the variability of vertical air motion. We note that part of the broader spread in the observed Doppler velocity may arise from observational uncertainties, such as beamwidth-related variability and multiple scattering. In addition, the retrieval of air motion is more uncertain in mixed-phase regions and under strong attenuation. These factors may contribute to the wider observed distributions. However, such uncertainties are unlikely to fully account for the marked reduction in variability in the simulations. These results suggest that the simulations produce overly constrained structures of radar reflectivity and Doppler velocity, which may be related to both limited resolution

https://doi.org/10.5194/egusphere-2026-2530
Preprint. Discussion started: 8 May 2026

and the parameterized representation of cloud microphysical processes. We further note that the simulations do not exhibit double peaks in air velocity with a minimum near the melting level, a characteristic of the EarthCARE air velocity retrieval data (Figs. 5, 10g). This is why we infer that the air-velocity retrieval may be subject to uncertainties near the melting level.

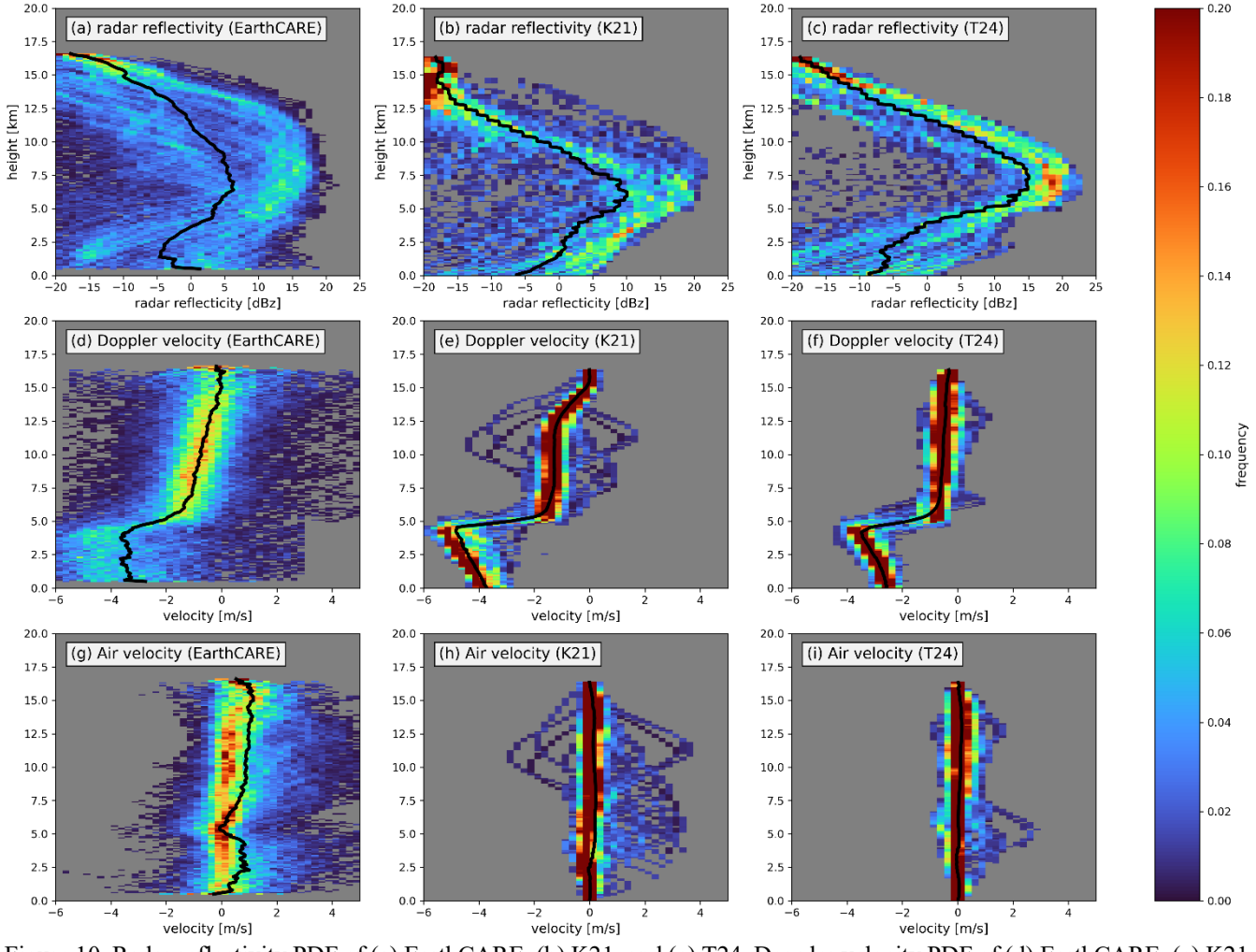

Figure 10. Radar reflectivity PDF of (a) EarthCARE, (b) K21, and (c) T24. Doppler velocity PDF of (d) EarthCARE, (e) K21, and (f) T24. Air velocity PDF of (g) EarthCARE, (h) K21, and (i) T24. The black lines are the mean of each variable.

https://doi.org/10.5194/egusphere-2026-2530
Preprint. Discussion started: 8 May 2026

We further evaluate the distributions of cloud water and ice content in NICAM simulations. Cloudy grid points with at least 0.001 g m^{-3} of liquid or ice water content are sampled to construct the PDFs (Fig. 11). The liquid water content retrieved from EarthCARE is generally smaller than 0.1 g m^{-3}, with a long tail extending toward 1 g m^{-3} (Fig. 11a). Both K21 and T24 capture this general pattern, although the frequency of the long tail is lower than in the observations (Fig. 11b and 11c). The mean profiles in K21 and T24 follow the observed structure reasonably well below 6 km. Above this level, liquid clouds are rarely observed, whereas non-negligible liquid water content persists in both simulations. This may suggest that NICAM tends to produce excessive supercooled liquid water. However, due to uncertainties in retrievals within mixed-phase regions, it is difficult to determine whether this represents a model bias.

Above the freezing level, the PDF of cloud ice content from EarthCARE at 5 km exhibits a skewed distribution with a long tail toward 1 g m^{-3}. With increasing height, the PDFs become more concentrated around ~0.1 g m^{-3} (Fig. 11d). In K21, the PDF peaks near 0.05 g m^{-3}, and the skewed structure is mainly confined between 5 and 10 km (Fig. 11e), which is narrower compared to the observation. In contrast, T24 exhibits a much broader PDF without a distinct peak, with ice content spanning from ~0.05 g m^{-3} to beyond 1.5 g m^{-3} (Fig. 11f). Both K21 and T24 overestimate the mean ice content relative to EarthCARE. These results indicate that reduced terminal velocity coefficients in T24 enhance the variability of cloud ice content, although the mean values remain overestimated. The comparison suggests that hydrometeor fall speed strongly influences the variability and the vertical distribution of cloud ice, which in turn affects the simulated reflectivity and Doppler velocity. The observational constraints offer guidance for improving the representation of cloud microphysical processes in models.

https://doi.org/10.5194/egusphere-2026-2530
Preprint. Discussion started: 8 May 2026

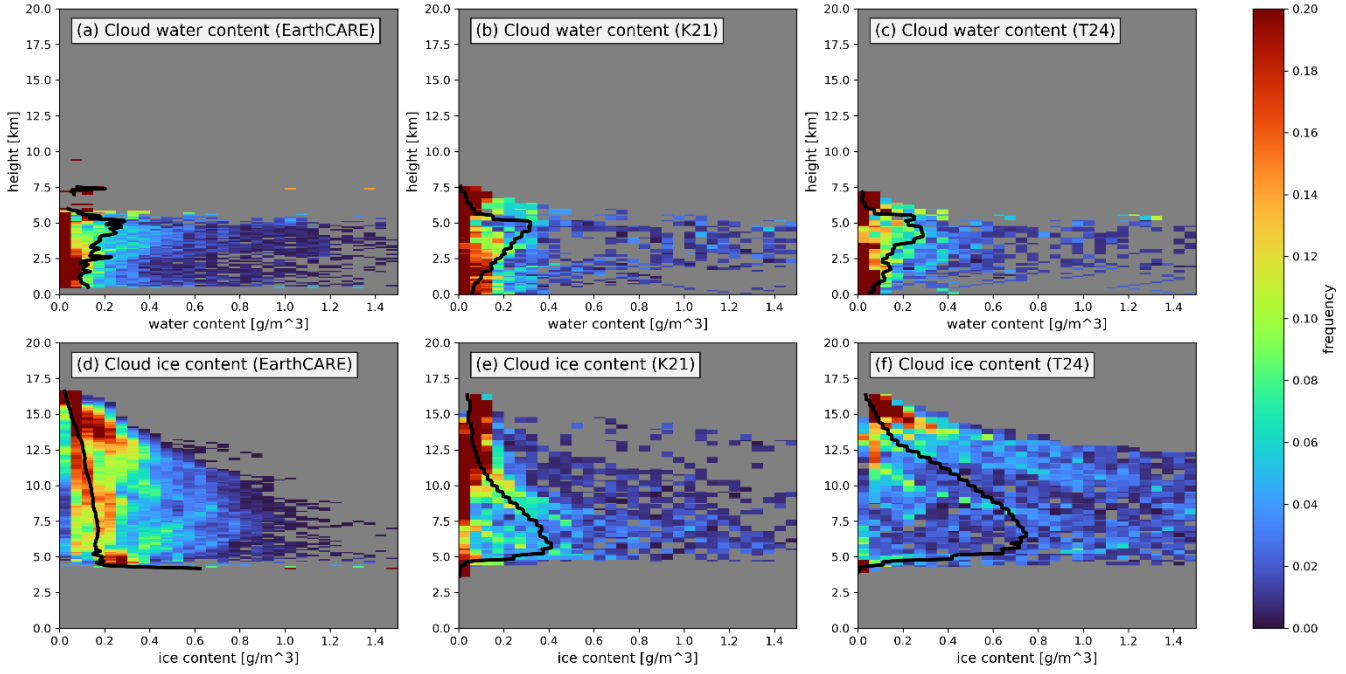

Figure 11. Cloud water content PDF of (a) EarthCARE, (b) K21, and (c) T24. Cloud ice content PDF of (d) EarthCARE, (e) K21, and (f) T24. The black lines are the mean of each variable.

4 Summary

This study uses unprecedented EarthCARE observations to investigate the dynamical and cloud microphysical structures of TCs. By co-locating EarthCARE overpasses with TC tracks, we construct statistics of the radial-height structures of radar reflectivity, Doppler velocity, air vertical motion, and cloud particle types. This provides a unique opportunity to examine the coupling between dynamics and cloud microphysics in TCs, which would not be possible without Doppler velocity observations from space. The observational results reveal a transition in TC structure from convective in the eyewall region to stratiform in the rainband region. The eyewall is characterized by strong updrafts, enhanced reflectivity, and broader variability in Doppler velocity. In contrast, the rainband region exhibits weaker vertical motion, a significant bright band signal near the melting level, and Doppler velocity distributions more strongly influenced by particle terminal velocity. The outer region generally shows weaker signals than the rainband region. These results indicate that Doppler velocity provides an effective constraint on the relative contributions of air motion and hydrometeor fall speed, linking dynamical and cloud microphysical processes across different TC regions. The distributions of cloud particle types further support the transition between the eyewall and rainband regions, consistent with the observed transition from a convective to a stratiform regime.

https://doi.org/10.5194/egusphere-2026-2530
Preprint. Discussion started: 8 May 2026

The analysis of cloud particle types in TCs provides a new perspective on cloud microphysical structure and its relationship with Doppler velocity, although uncertainties remain in the retrieval. In particular, our results suggest that mixed-phase particles occur more frequently than previously reported, even above 6 km where temperatures are below −5°C, which contrasts with earlier studies (e.g., Black et al., 1999). The increased occurrence of mixed-phase particles implies that supercooled water may be more prevalent in TCs than inferred from earlier aircraft observations (e.g., Willoughby et al., 1985). EarthCARE offers a unique opportunity to better understand the amount of supercooled water in TCs and associated structure of air motions. Further comparisons with ground-based radar observations will help to reduce uncertainties and improve the robustness of these findings.

The NICAM hindcast simulations of Hurricane Humberto reproduce TC tracks and overall TC structure, but underestimate TC intensity. The simulated distributions of radar reflectivity, Doppler velocity, and air vertical motion are generally more confined than those observed by EarthCARE, suggesting limited variability in both dynamical and cloud microphysical fields. Differences between simulations with two different terminal-velocity settings in the cloud microphysics scheme further highlight the role of hydrometeor fall speed in shaping the vertical structure of reflectivity and Doppler velocity. These results suggest that cloud microphysical assumptions, particularly those related to particle fall speeds, strongly control the simulated structure and variability of clouds in TCs. The improvements in track and intensity remain limited in this case, and the simulated results may depend on the large-scale environment, the internal TC structure and the spin-up processes. We will investigate additional TC cases with various lead times to enable a more robust statistical comparison.

In conclusion, this study presents a new observational perspective on contrasting dynamics and cloud microphysical structures in TCs using EarthCARE observations. The hindcast simulation results for Humberto and their comparison with EarthCARE observations highlight the importance of representing both the variability and the vertical structure of cloud and precipitation processes in models. The observational constraints offer valuable guidance for improving the representation of cloud microphysical processes and their coupling with dynamics in a global km-scale storm-resolving model.

Code and data availability

The EarthCARE data used in this study are available from the JAXA G-Portal (https://gportal.jaxa.jp/gpr/index/index), including CPR (https://doi.org/10.57746/EO.01jdvd2gqq34e6yz9p8kfe68x5) and CPR-ATLID synergistic (https://doi.org/10.57746/EO.01jkwjeg2y0bqndnsvjvaaskaw) Level-2 products. IMERG dataset can be found in https://gpm.nasa.gov/data/imerg, and 3-year IBTrACS is downloaded from https://doi.org/10.25921/82ty-9e16. J-Sim used to generate satellite-like signals from NICAM outputs is available from JAXA (https://www.eorc.jaxa.jp/theme/Joint-

https://doi.org/10.5194/egusphere-2026-2530
Preprint. Discussion started: 8 May 2026

Simulator/userform/js_userform.html). The processed dataset supporting the findings of this study is publicly available at figshare repository (https://doi.org/10.6084/m9.figshare.32142271).

Author contributions

J.-D. H.: Conceptualization, Methodology, Formal analysis, Data curation, Investigation, Writing – original draft.
W. R.: Conceptualization, Methodology, Formal analysis, Writing – review & editing.
M. S.: Conceptualization, Supervision, Funding acquisition, Writing – review & editing.
T. M.: Conceptualization, Supervision, Writing – review & editing.

Competing interests

The authors declare that they have no conflict of interest.

Acknowledgements

The authors thank members of the JAXA EarthCARE Science Team and the J-Sim project. The authors used ChatGPT (OpenAI) to assist with English language editing to improve clarity and reduce potential language barriers.

Financial support

This work was supported by the EarthCARE satellite study commissioned by the Japan Aerospace Exploration Agency, the Moonshot R&D Grant JPMJMS2282-02 from the Japan Science and Technology Agency, JSPS Core-to-Core Program (grant

number: JPJSCCA20220001), JSPS KAKENHI Grant Number 24K00703, 24H02228 and JP24H00275. The NICAM simulations in this study were performed on the supercomputer Fugaku (proposal numbers hp250068, hp250179, hp260066). We also thank the joint research program of the Institute for Space-Earth Environmental Research (ISEE), Nagoya University.

References

Baker, A. J., Vannière, B., and Vidale, P. L.: On the realism of tropical cyclone intensification in global storm-resolving climate models, Geophys. Res. Lett., 51, e2024GL109841, https://doi.org/10.1029/2024GL109841, 2024.

Black, R. A. and Hallett, J.: Observations of the distribution of ice in hurricanes, J. Atmos. Sci., 43, 802–822, https://doi.org/10.1175/1520-0469(1986)043<0802:OOTDOI>2.0.CO;2, 1986.

Black, R. A. and Hallett, J.: Electrification of the hurricane, J. Atmos. Sci., 56, 2004–2028, https://doi.org/10.1175/1520-0469(1999)056<2004:EOTH>2.0.CO;2, 1999.

Black, R. A., Heymsfield, G. M., and Hallett, J.: Extra large particle images at 12 km in a hurricane eyewall: Evidence of high-altitude supercooled water?, Geophys. Res. Lett., 30, https://doi.org/10.1029/2003GL017864, 2003.

Dvorak, V. F.: Tropical cyclone intensity analysis and forecasting from satellite imagery, Mon. Weather Rev., 103, 420–430, https://doi.org/10.1175/1520-0493(1975)103<0420:TCIAAF>2.0.CO;2, 1975.

Dvorak, V. F.: Tropical cyclone intensity analysis using satellite data, NOAA, available at: https://repository.library.noaa.gov/view/noaa/19322 (last access: 24 April 2026), 1984.

Gahtan, J., Knapp, K. R., Schreck, C. J., Diamond, H. J., Kossin, J. P., and Kruk, M. C.: International Best Track Archive for Climate Stewardship (IBTrACS) Project, Version 4r01, NOAA National Centers for Environmental Information, https://doi.org/10.25921/82ty-9e16, 2025.

Hashino, T., Satoh, M., Hagihara, Y., Kubota, T., Matsui, T., Nasuno, T., and Okamoto, H.: Evaluating cloud microphysics from NICAM against CloudSat and CALIPSO, J. Geophys. Res., 118, 7273–7292, https://doi.org/10.1002/jgrd.50564, 2013.

https://doi.org/10.5194/egusphere-2026-2530
Preprint. Discussion started: 8 May 2026

Hersbach, H., Bell, B., Berrisford, P., Hirahara, S., Horányi, A., Muñoz-Sabater, J., and Thépaut, J.-N.: The ERA5 global reanalysis, Q. J. R. Meteorol. Soc., 146, 1999–2049, https://doi.org/10.1002/qj.3803, 2020.

Huffman, G. J., Bolvin, D. T., Braithwaite, D., Hsu, K. L., Joyce, R. J., Kidd, C., and Xie, P.: Integrated multi-satellite retrievals for the Global Precipitation Measurement (GPM) mission (IMERG), in: Satellite Precipitation Measurement, Springer, Cham, 343–353, https://doi.org/10.1007/978-3-030-24568-9_19, 2020.

Illingworth, A. J., Barker, H. W., Beljaars, A., Ceccaldi, M., Chepfer, H., Clerbaux, N., and Van Zadelhoff, G. J.: The EarthCARE satellite: The next step forward in global measurements of clouds, aerosols, precipitation, and radiation, Bull. Am. Meteorol. Soc., 96, 1311–1332, https://doi.org/10.1175/BAMS-D-12-00227.1, 2015.

Judt, F., Klocke, D., Rios-Berrios, R., Vannière, B., Ziemen, F., Auger, L., and Zhou, L.: Tropical cyclones in global storm-resolving models, J. Meteorol. Soc. Jpn., 99, 579–602, https://doi.org/10.2151/jmsj.2021-029, 2021.

Knapp, K. R., Kruk, M. C., Levinson, D. H., Diamond, H. J., and Neumann, C. J.: The International Best Track Archive for Climate Stewardship (IBTrACS): Unifying tropical cyclone data, Bull. Am. Meteorol. Soc., 91, 363–376, https://doi.org/10.1175/2009BAMS2755.1, 2010.

Kodama, C., Ohno, T., Seiki, T., Yashiro, H., Noda, A. T., Nakano, M., and Sugi, M.: The Nonhydrostatic Icosahedral Atmospheric Model for CMIP6 HighResMIP simulations (NICAM16-S), Geosci. Model Dev., 14, 795–820, https://doi.org/10.5194/gmd-14-795-2021, 2021.

Lee, T. Y. and Wing, A. A.: Satellite-based estimation of the role of cloud–radiative interaction in accelerating tropical cyclone development, J. Atmos. Sci., 81, 959–982, https://doi.org/10.1175/JAS-D-23-0142.1, 2024.

Luo, Z., Stephens, G. L., Emanuel, K. A., Vane, D. G., Tourville, N. D., and Haynes, J. M.: On the use of CloudSat and MODIS data for estimating hurricane intensity, IEEE Geosci. Remote Sens. Lett., 5, 13–16, https://doi.org/10.1109/LGRS.2007.905341, 2008.

Okamoto, H., Sato, K., Nishizawa, T., Jin, Y., Nakajima, T., Wang, M., and Tanaka, T.: JAXA Level 2 algorithms for EarthCARE mission from single to four sensors: New perspective of cloud, aerosol, radiation and dynamics, Atmos. Meas. Tech. Discuss., https://doi.org/10.5194/amt-2024-101, 2024.

https://doi.org/10.5194/egusphere-2026-2530
Preprint. Discussion started: 8 May 2026

Reynolds, R. W., Rayner, N. A., Smith, T. M., Stokes, D. C., and Wang, W.: An improved in situ and satellite SST analysis for climate, J. Climate, 15, 1609–1625, https://doi.org/10.1175/1520-0442(2002)015<1609:AIISAS>2.0.CO;2, 2002.

Roh, W. and Satoh, M.: Evaluation of precipitating hydrometeor parameterizations in a single-moment bulk microphysics scheme for deep convective systems, J. Atmos. Sci., 71, 2654–2673, https://doi.org/10.1175/JAS-D-13-0252.1, 2014.

Roh, W., Satoh, M., Hashino, T., Okamoto, H., and Seiki, T.: Evaluations of the thermodynamic phases of clouds in a cloud-system-resolving model using CALIPSO, J. Atmos. Sci., 77, 3781–3801, https://doi.org/10.1175/JAS-D-19-0273.1, 2020.

Roh, W., Satoh, M., Matsugishi, S., Aoki, S., Kubota, T., and Okamoto, H.: Vertical motions in clouds from EarthCARE satellite and a global storm-resolving modeling, Sci. Rep., https://doi.org/10.1038/s41598-025-32256-8, 2025.

Sato, K., Okamoto, H., Yamamoto, M. K., Fukao, S., Kumagai, H., Ohno, Y., and Abo, M.: 95-GHz Doppler radar and lidar synergy for simultaneous ice microphysics and in-cloud vertical air motion retrieval, J. Geophys. Res., 114, D03203, https://doi.org/10.1029/2008JD010222, 2009.

Sato, K., Okamoto, H., Nishizawa, T., Jin, Y., Nakajima, T. Y., Wang, M., and Kudo, R.: JAXA Level 2 cloud and precipitation microphysics retrievals based on EarthCARE radar, lidar, and imager: The CPR_CLP, AC_CLP, and ACM_CLP products, Atmos. Meas. Tech., 18, 1325–1338, https://doi.org/10.5194/amt-18-1325-2025, 2025.

Satoh, M., Matsuno, T., Tomita, H., Miura, H., Nasuno, T., and Iga, S.: Nonhydrostatic icosahedral atmospheric model (NICAM) for global cloud resolving simulations, J. Comput. Phys., 227, 3486–3514, https://doi.org/10.1016/j.jcp.2007.02.006, 2008.

Satoh, M., Stevens, B., Judt, F., Khairoutdinov, M., Lin, S. J., Putman, W. M., and Düben, P.: Global cloud-resolving models, Curr. Clim. Change Rep., 5, 172–184, https://doi.org/10.1007/s40641-019-00131-0, 2019.

Satoh, M., Tomita, H., Yashiro, H., Miura, H., Kodama, C., Seiki, T., and Kubokawa, H.: The non-hydrostatic icosahedral atmospheric model: Description and development, Prog. Earth Planet. Sci., 1, 18, https://doi.org/10.1186/s40645-014-0018-1, 2014.

Sekiguchi, M. and Nakajima, T.: A k-distribution-based radiation code and its computational optimization for an atmospheric general circulation model, J. Quant. Spectrosc. Radiat. Transfer, 109, 2779–2793, https://doi.org/10.1016/j.jqsrt.2008.07.013, 2008.

https://doi.org/10.5194/egusphere-2026-2530
Preprint. Discussion started: 8 May 2026

Stevens, B., Acquistapace, C., Hansen, A., Heinze, R., Klinger, C., Klocke, D., and Zängl, G.: The added value of large-eddy and storm-resolving models for simulating clouds and precipitation, J. Meteorol. Soc. Jpn., 98, 395–435, https://doi.org/10.2151/jmsj.2020-021, 2020.

Stevens, B., Satoh, M., Auger, L., Biercamp, J., Bretherton, C. S., Chen, X., and Zhou, L.: DYAMOND: The dynamics of the atmospheric general circulation modeled on non-hydrostatic domains, Prog. Earth Planet. Sci., 6, 61, https://doi.org/10.1186/s40645-019-0304-z, 2019.

Takasuka, D., Kodama, C., Suematsu, T., Ohno, T., Yamada, Y., Seiki, T., and Masunaga, R.: How can we improve the seamless representation of climatological statistics and weather?, J. Adv. Model. Earth Syst., 16, e2023MS003701, https://doi.org/10.1029/2023MS003701, 2024.

Takata, K., Emori, S., and Watanabe, T.: Development of the minimal advanced treatments of surface interaction and runoff, Glob. Planet. Change, 38, 209–222, https://doi.org/10.1016/S0921-8181(03)00030-4, 2003.

Tomita, H. and Satoh, M.: A new dynamical framework of nonhydrostatic global model using the icosahedral grid, Fluid Dyn. Res., 34, 357–400, https://doi.org/10.1016/j.fluiddyn.2004.03.003, 2004.

Tomita, H.: New microphysical schemes with five and six categories by diagnostic generation of cloud ice, J. Meteorol. Soc. Jpn., 86, 121–142, https://doi.org/10.2151/jmsj.86A.121, 2008.

Tourville, N., Stephens, G., DeMaria, M., and Vane, D.: Remote sensing of tropical cyclones: Observations from CloudSat and A-Train profilers, Bull. Am. Meteorol. Soc., 96, 609–622, https://doi.org/10.1175/BAMS-D-13-00282.1, 2015.

Wehr, T., Kubota, T., Tzeremes, G., Wallace, K., Nakatsuka, H., Ohno, Y., and Bernaerts, D.: The EarthCARE mission – Science and system overview, Atmos. Meas. Tech., 16, 3581–3608, https://doi.org/10.5194/amt-16-3581-2023, 2023.

Willoughby, H. E., Jorgensen, D. P., Black, R. A., and Rosenthal, S. L.: Project STORMFURY: A scientific chronicle 1962–1983, Bull. Am. Meteorol. Soc., 66, 505–514, https://doi.org/10.1175/1520-0477(1985)066<0505:PSASC>2.0.CO;2, 1985.

Wu, S. N. and Soden, B. J.: Signatures of tropical cyclone intensification in satellite measurements of ice and liquid water content, Mon. Weather Rev., 145, 4081–4091, https://doi.org/10.1175/MWR-D-17-0046.1, 2017.

https://doi.org/10.5194/egusphere-2026-2530
Preprint. Discussion started: 8 May 2026

Wu, S. N., Soden, B. J., and Alaka, G. J.: Ice water content as a precursor to tropical cyclone rapid intensification, Geophys. Res. Lett., 47, e2020GL089669, https://doi.org/10.1029/2020GL089669, 2020.